First-principles study on the interfacial cathode-contact stability and Li diffusivity of N-doped $Li_6Zr_2O_7$ for all-solid-state Li-ion batteries

Randy Jalem[1,*], Yoshitaka Tateyama[1], Kazunori Takada[1], Tetsuya Yamada[2], Katsuya Teshima[2,3]
[1]Research Center for Energy and Environmental Materials (GREEN), National Institute for Materials Science (NIMS), 1-1 Namiki, Tsukuba, Ibaraki 305-0044, Japan
[2]Department of Materials Chemistry, Faculty of Engineering, Shinshu University, 4-17-1 Wakasato, Nagano 380-8553, Japan
[3]Institute for Aqua Regeneration, Shinshu University, 4-17-1 Wakasato, Nagano 380-8553, Japan

Email: JALEM.Randy@nims.go.jp

Abstract

Here, N-doped $Li_6Zr_2O_7$ (LZON) was investigated using first-principles density functional theory (DFT) methods to evaluate its (electro)chemical stability and Li-ion transport properties for its novel design as a practical dual-use Li ionic conductor, both as a cathode-coating layer (CCL) and solid electrolyte (SE) in all-solid-state Li-ion batteries (ASSBs). Thermodynamic free energy calculations showed that LZO is chemically stable vs. most known cathode materials. Focusing on $LiCoO_2$ (LCO) cathode, explicit hetero-interface modeling analysis of the low-energy LCO(104)|LZO(001) interface revealed that LZO can form a strongly adhered and a low-strain contact with LCO. The electronic structure of this interface has LCO-side states (Co-3d, O-2p) occupying the highest occupied states, thereby facilitating a stable cell charging. Climbing-image nudged elastic band calculations results suggested that the LCO(104)|LZO(001) interface also has interface-normal diffusion pathways with low Li ion migration energy. Meanwhile, *ab-initio*- and machine-learning-based molecular dynamics simulation results confirmed that Li diffusivity in bulk LZO can be greatly enhanced by several orders of magnitude via aliovalent N-doping with Li interstitial addition. For the LCO(104)|LZON(001) interface, the N dopant is determined to energetically prefer the LZON bulk region, the corresponding interface electronic structure that can also facilitate a stable cell charging.

Introduction

Oxide-type Li-ion conductors (OLCs) with excellent electrochemical stability and high Li diffusivity are amongst the strongly sought materials for the development of highly practical all-solid-state Li-ion batteries (ASSBs). They demonstrate good chemical stability and high safety when used as battery components such as solid electrolytes (SEs), interphase buffer layers and cathode coating layer (CCL) materials.[1-2] As SEs, OLCs with exceptionally high Li-ion conductivity (σ_{Li}) have been reported: garnets (e.g., $Li_7La_3Zr_2O_{12}$),[3] perovskites (e.g., $Li_{0.375}Sr_{0.4375}Ta_{0.75}Zr_{0.25}O_3$),[4] NASICONs (e.g., $Li_{1.3}Al_{0.3}Ti_{1.7}(PO_4)_3$, $Li_{1.5}Al_{0.5}Ge_{1.5}(PO_4)_3$),[5-6] and oxyhalides (e.g., $LiNbOCl_4$, pyrochlore-type

$Li_{1.25}La_{0.58}Nb_2O_6F$)[7-8]. As buffer layers and CCLs, OLCs have been employed to address issues such as interfacial instability, contact loss and high cell impedance that result in poor battery rate capability and cycle performance in solid-state cells. Some examples include Li_3PO_4 as a buffer layer for the $LiCoO_2$ (LCO) cathode – Li_3PS_4 SE interface in thin-film ASSBs,[9] Li_3BO_3 as a sintering additive for the LCO cathode – $Li_7La_3Zr_2O_{12}$ SE interface,[10] surface modifiers such as Al_2O_3 and ZnO on $Li_7La_3Zr_2O_{12}$ SE and SnO_2 on $Li_{1.5}Al_{0.5}Ge_{1.5}(PO_4)_3$ SE in the anode side (i.e., with Li metal contact),[11-13] and oxide CCLs such as TiO, $LiNbO_3$, and $Li_6Zr_2O_7$[14-16].

Recently, an enhanced electrochemical performance of Ni-rich $LiNi_{0.8}Co_{0.1}Mn_{0.1}O_2$ (NCM811) cathode by $Li_6Zr_2O_7$ (LZO) CCL was reported.[16] The beneficial effect of LZO was claimed to be related to the induced delay in temperature-driven phase transition (layer R-3m → spinel Fd-3m, rocksalt Fm-3m) and the suppressed interfacial degradation of the NCM811 cathode. In NCM cathodes, particularly for degradation-susceptible high-Ni content compositions, oxygen release and large volume change are two of the reported significant degradation mechanisms that can lead to capacity fade and thermal runaway.[17]

The crystal structure of LZO is shown in Figure 1, it belongs to monoclinic symmetry and a $C2/c$ space group. The host framework has pairs of edge-shared ZrO_6 octahedral units (Zr 8f Wyckoff site, O 4e and 8f Wyckoff site) which are corner-shared with other neighboring edged-shared ZrO_6 units. Li ions (8f Wyckoff site) are located at square pyramidal interstitial sites (i.e., as LiO_5 units). The total σ_{Li} of LZO was experimentally measured at 573 K to be on the order of $\sim 10^{-5}$ S cm^{-1}, while its Li activation energy was estimated to be ~1 eV.[18-19] In these works, the σ_{Li} measurement of the material required elevated temperatures, suggesting poor Li diffusivity that makes LZO unattractive for SE use. Meanwhile, an almost two orders of magnitude enhancement in σ_{Li} at the same elevated temperatures was achieved by aliovalent cation substitution (e.g., Y^{3+}) at the LZO Zr^{4+} site, with inclusion of extra interstitial Li for charge compensation.[19] The bulk Li diffusion pathways and barriers of LZO had been investigated computationally as well by bond softness analysis, predicting the presence of Li pathways with low energy barriers (0.35 – 0.45 eV).[20] These results appear to be somewhat consistent with the reported improved electrochemical performance of cathodes with LZO CCL, but they are inconsistent with the experimentally measured σ_{Li} of LZO. The Li ion transport in LZO CCL can differ from the bulk-dominated diffusion process, as microstructure contributions become dominant at the relevant scale (e.g., grain nano-sizing, mechanical stress and strain, amorphization, formation of interphases, and composition stoichiometry deviation). Depending on the dominant contributions and their interplay, Li diffusivity in LZO can then either be diminished or enhanced. From these points, it is evident that there are still gaps in the understanding about the interface-related and Li diffusion properties of LZO.

Here, the cathode-contact (electro)chemical stability and Li diffusivity of N-doped LZO (LZON) are investigated by first-principles density functional theory (DFT) methods. Thermodynamic analysis is performed based on Gibbs free energy calculations to study the phase stability and cathode-contact bulk reactivity of the material. To study the interfacial electronic and Li ion transport properties of LZO(N) as a CCL, DFT thermodynamic and Li ion migration calculations and analyses using explicit hetero-interface structure models are carried out, with LCO as the cathode material. The bulk Li diffusivity was also studied by *ab-initio* and machine-learning-based molecular dynamics (AIMD, ML-MD) methods to determine the viability of N-doping in LZO for enhancing bulk σ_{Li}. Overall, our results offer valuable insights on the design and fundamental understanding of OLCs for CCL and SE applications in ASSBs.

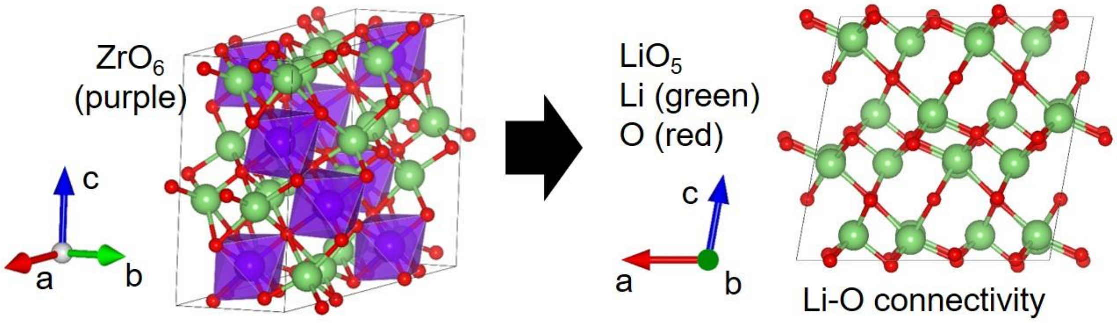

Figure 1. Crystal structure of monoclinic *C*2/*c* $Li_6Zr_2O_7$ (LZO). Each ZrO_6 unit (purple) is characterized by 3 O vertices (red) that are corner-shared with neighboring ZrO_6 units and 2 O vertices in an edge-sharing configuration with a neighboring ZrO_6 unit. Li atoms (green) are coordinated in a square pyramidal configuration (i.e., LiO_5).

Calculation details

Structure relaxation

The VASP software[21-22] is used for DFT calculations in this work, it employs the projector augmented wave (PAW) method[23-25]. The DFT + U scheme within the generalized gradient approximation of the Perdew, Burke, and Ernzernhof functional (GGA-PBE) is implemented.[26-27] The experimental crystal coordinate data of *C*2/*c* LZO and *R*-3*m* $LiCoO_2$ (LCO) are taken from previous experimental works.[28-29] For LCO, the Hubbard U value is set to 3.32 eV for the Co-3d state.[30] For pseudopotentials, the following valence configurations are chosen: $1s^22s^1$ for Li, $4s^24p^64d^35s^1$ for Zr, $3d^84s^1$ for Co, $2s^22p^4$ for O, and $2s^22p^3$ for N. The cutoff for kinetic energy is set to 520 eV and the k-points resolution is fixed to at least 1000 in a Monkhorst-Pack grid scheme;[31] spin polarization is switched on. For energy and residual force convergences, the criteria are set to <1 meV/atom and <0.01 eV/Å, respectively.

For the N-doped LZO (LZON) structure, the unit cell is expanded into a 1 x 2 x 1 supercell, resulting to a structure model with > 10 Å in cell edges. Two doping cases are considered: (i) N at the O site (x = [1, 2, 3, 4, 5, 6, 7] in $Li_{48+x}Zr_{16}O_{56-x}N_x$) and (b) N at the interstitial site (x = [1] in $Li_{48+3x}Zr_{16}O_{56}N_x$).

Extra Li atoms are added for charge compensation. The vacancy/interstitial sites for the dopant N^{3-} and extra Li^+ are searched by an algorithm based on DFT electronic charge density analysis (Fig. S1).[32] A total of 500 Li-O-N-vacancy configurations are randomly sampled for each N content. These sampled structures are then sorted based on electrostatic Ewald energy (E_{Ewald}) criterion. The top-5 unique lowest-E_{Ewald} structures are selected and subjected to DFT structure relaxation, the one with the lowest DFT total energy (E_0) is then chosen as the representative structure for use in further analyses/calculations.

Evaluation of thermodynamic phase stability

The thermodynamic phase stability of LZO(N) is evaluated using the DFT decomposition energy (E_{d}) metric which can be calculated by convex hull approach.[33] The thermodynamic decomposition energy, E_{d} (eV atom^{-1}), is calculated according to the following formula:

$$E_{\text{d}} = \Delta H_{\text{f}} - \Delta H_c, \qquad (1)$$

where ΔH_{f} and ΔH_{c} are the convex hull energies related to the target phase/compound and the phase equilibria at composition c (i.e., the thermodynamically stable competing phases), respectively.

The bulk cathode-contact stability of a target compound (e.g., LZO) is determined based on the interfacial minimum mutual reaction energy, $\Delta E_{\text{mutual,min}}$:[34]

$$\Delta E_{\text{mutual,min}} = \min_{x\in[0,1]}\{\frac{1}{N}[E_{\text{eq}}(xc_{\text{A}} + (1-x)c_{\text{B}}) - xE(c_{\text{A}}) - (1-x)E(c_{\text{B}})]\} \quad (2)$$

where x and $(1-x)$ are the ratios in the pseudo-binary phase diagram of cathode A and target compound B, respectively, $E(c_{\text{A}})$ and $E(c_{\text{B}})$ are the DFT total energies at the convex hull at cathode A and target compound B compositions, respectively, $E_{\text{eq}}(xc_{\text{A}} + (1-x)c_{\text{B}})$ is the phase equilibria energy at composition $xc_{\text{A}} + (1-x)c_{\text{B}}$, and N is the total number of atoms involved in a given reaction.

The total energy data of relevant competing phases are taken from the Materials Project database and the corresponding phase diagrams were constructed using the pymatgen library.[35-36]

Interface structure search of cathode – coating contact

The explicit-interface cathode-contact stability of LZO is analyzed by constructing an LCO|LZO interface structure model. The LCO (104) surface is chosen as the representative cathode facet contact, this choice is based on previous works that analyzed the surface stability and favorable Li pathways of the material (Fig. S2).[37] For the LZO CCL, several non-polar, symmetric facet surfaces are constructed (Fig. S3). The following equation is used to calculate surface energy ($\gamma_{surface}$):

$$\gamma_{surface} = \frac{E_{slab} - E_{bulk}}{2A}, \qquad (3)$$

where E_{slab}, E_{bulk}, and A are the DFT total energy of the surface slab structure, DFT total energy of the bulk structure, and surface area, respectively.

To generate the LCO|LZO interface model, a superlattice-matching strategy that creates coherent interfaces of LCO and LZO surfaces is employed, as implemented in the pymatgen package.[36, 38] A maximum tolerance length, angle and superlattice area of 0.1 Å, 0.1° and 300 Å^2, respectively, were considered during the interface generation step. The generated interfaces are further optimized in the contact-lateral and contact-normal directions using Bayesian optimization which is coupled to the DFT structure relaxation routine (BO+DFT method, see Fig. S4 for the calculation workflow), the goal is to efficiently find the shifted LCO|LZO interface with the lowest DFT total energy after relaxation (i.e., minimizing the objective function, $f_{LCO|LZO}$). A 3D grid of lateral and vertical interface shifts (i.e., the search space $\boldsymbol{X}$) is defined with a 0.25-Å shift interval in the ranges of [0, 3 Å] and [0, 0.75 Å], respectively, where $\boldsymbol{x}$ = (0, 0, 0) coordinate represents the initial coherent interface. A Gaussian Process (GP) model for $f_{LCO|LZO}$ is constructed with a radial basis function kernel. The error loss function is formulated based on mean square error (MSE) which is minimized using the Adam optimizer with a learning rate of 0.01. The Expected Improvement (EI) acquisition function is used to decide which of the shifted LCO|LZO structure candidates should be geometry-relaxed next by DFT calculation.[39] For the initial training dataset (i.e., DFT total energy), 3 interfaces are randomly sampled (from $\boldsymbol{X}$) and subjected to DFT geometry optimization. The BO sampling iteration is terminated when $f_{LCO|LZO}$ does not change for the next 2 BO steps, the lowest-energy interface is then chosen as the representative LCO|LZO interface for further analyses.

The work of adhesion (W_{adhesion}) of the LCO|LZO interface is determined using the following formula:

$$W_{\mathrm{adhesion}} = \frac{1}{A_{\mathrm{LCO-LZO}}}\left(E_{\mathrm{LCO|LZO}} - E_{\mathrm{LCO\ slab}} - E_{\mathrm{LZO\ slab}}\right), \qquad (4)$$

where $E_{\mathrm{LCO|LZO}}$, $E_{\mathrm{LCO\ slab}}$, $E_{\mathrm{LZO\ slab}}$, and $A_{\mathrm{LCO|LZO}}$ are LCO|LZO structure, LCO slab, LZO slab total energies, and LCO|LZO interface area, respectively.

For the LCO|LZON interface, the DFT-geometry-optimized LCO(104)|LZO(001) interface is used as the structure template. Two models are considered, each with 1 dopant anion in the LZO slab side: (i) N^{3-} at an LZO-side surface O^{2-} site and (ii) N^{3-} at an O^{2-} site that is away from the interface (i.e., in the LZO bulk region). In both cases, one extra Li^+ is added at an interstitial site near the N^{3-} for charge compensation. The resulting LCO(104)|LZON(001) interface is then subjected to DFT geometry optimization and post-processing analyses.

Ion dynamics simulations and analysis

AIMD simulations for bulk LZO and LZON (at x = 0.5 in $Li_{6+x}Zr_2O_{7-x}N_x$) are carried out using a 1 x 2 x 1 supercell with a 1-fs MD step size. To estimate the bulk Li ion activation energy (E_a), the Arrhenius plot is determined using the Li diffusivity data at 600, 800, 1000, 1200, and 1400 K. Under NPT ensemble condition,[40] a structure equilibration step at each MD temperature is performed for 20 ps, this is then followed by the MD production run with a trajectory length of 100 ps.

To investigate the effects of N-doping content to bulk σ_{Li} at 300 K, direct MD calculations are performed using a fitted machine learning interatomic potential (MLIP) based on scalable sparse Gaussian process regression formalism with training and test datasets from AIMD trajectories, using the autoforce package.[41-44] Other details of the MLIP training and testing procedure are provided in Supporting Information.

The time-averaged Li-ion mean square displacement (MSD) is calculated using the following equation:[45]

$$MSD = \langle [\boldsymbol{r}(t+\tau) - \boldsymbol{r}(t)]^2 \rangle, \qquad (5)$$

where $\boldsymbol{r}(t)$ is the Li position at time t and τ is the lag time. The Li diffusion coefficient (D) is estimated according to the Einstein-Smoluchowski equation:[46]

$$D = \lim_{t\to\infty} [(1/2dt)\langle [\boldsymbol{r}(t+\tau) - \boldsymbol{r}(t)]^2 \rangle], \qquad (6)$$

where d is the diffusion dimensionality of the Li ions. Here, D is derived from the diffusive-regime slope of the MSD plot. Using Nernst-Einstein relationship, the bulk σ_{Li} ($\sigma_{\mathrm{bulk,Li}}$) is calculated as follows:[47]

$$\sigma_{\mathrm{bulk,Li}} = \rho F_c^2 z_c^2 D / RT, \qquad (7)$$

where ρ is the Li mass density, z_c is the Li ion charge, F_c is the Faraday constant, R is the gas constant and T is the temperature.

The Li correlation and dynamical properties are analyzed using the van Hove equation ($G(\boldsymbol{r},t)$):

$$G(\boldsymbol{r},t) = \frac{1}{N}\langle \sum_{N}^{i=1} \delta(\boldsymbol{r} + \boldsymbol{r}_i(0) - \boldsymbol{r}_i(t)) \rangle + \frac{1}{N}\langle \sum_{N}^{i\neq j} \delta(\boldsymbol{r} + \boldsymbol{r}_j(0) - \boldsymbol{r}_i(t)) \rangle, \qquad (8)$$

where N, $\langle\cdot\rangle$ and $\delta(\cdot)$ are the total number of Li ions, the ensemble-averaged quantities and the 3D Dirac delta function, respectively. The first term accounts for the Li self-correlation $G_{\mathrm{self}}(\boldsymbol{r},t)$ while the second term represents the distinct Li-Li correlation ($G_{\mathrm{distinct}}(\boldsymbol{r},t)$).

Li-ion migration analysis at the cathode-coating interface region

The local Li-ion migration barriers at the LCO|LZO interface region are evaluated by climbing-image nudged elastic band (DFT-cNEB) method. The LCO- and LZO-side surface Li ions (sites) are considered as initial and final states, respectively, with vacancy mechanism as the Li transport model. Three intermediate images are generated for each local Li pathway.

Results and discussion

Structure and phase stability check

The convex-hull E_{d} value of LZO is determined to be 0 meV atom^{-1}, characterizing it as a ground-state phase. Meanwhile, it is noted that, for LZON structures, a positive correlation is found between Ewald energy and lower-bound DFT total energy (Fig. S5), validating the configuration sampling strategy in this work when finding low-energy structures. Fig. 2a shows the plot for E_{d} vs. N-doping content (i.e., at O site), there is a monotonically increasing relationship and thus a decreasing phase stability trend (i.e., up to E_d = 74.2 meV atom^{-1}). The predicted ground-state decomposition phases include LZO, Li_2ZrN_2 and Li_2O. For comparison, the case of LZO with one N^{3-} doped at an interstitial site (i.e., $Li_{6.375}Zr_2O_7N_{0.125}$) is also evaluated, it has E_d = 40.0 meV atom^{-1} which makes this configuration relatively less stable than in the case of N-doping at the O site (i.e., E_d = 15.3 meV atom^{-1} for $Li_{6.125}Zr_2O_{6.875}N_{0.125}$). Empirical observation shows that most of metastable and synthesizable oxides found in experimental structure databases typically fall within E_d < 100 meV atom^{-1}.[48]

Fig. 2b shows the $\Delta E_\mathrm{mutual,min}$ for the most exothermic reactions for different combinations of cathode and SE/SE-related phases. Here, the degree of reactivity is shown to be strongly composition-dependent. The most chemically reactive interfaces (i.e., $\Delta E_\mathrm{mutual,min}$ << 0) are determined for Li_2ZrN_2 (a decomposition product of LZON) and sulfide-type Li_3PS_4, especially when in contact with LCO and Ni-rich cathodes (NCM333, NCM811 and $LiNiO_2$). LZO is found to have relatively less-negative $\Delta E_\mathrm{mutual,min}$ values vs. most of the considered cathodes, except against polyanion-type ones such as $LiFePO_4$ and $Li_3V_2(PO_4)_3$. Li_2O (another decomposition product of LZON), shows a similar low cathode-contact reactivity trend as with LZO. Other SE phases such as halide-type Li_3YBr_6 and garnet $Li_7La_3Zr_2O_{12}$ are also found to be relatively less reactive, similar to LZO.

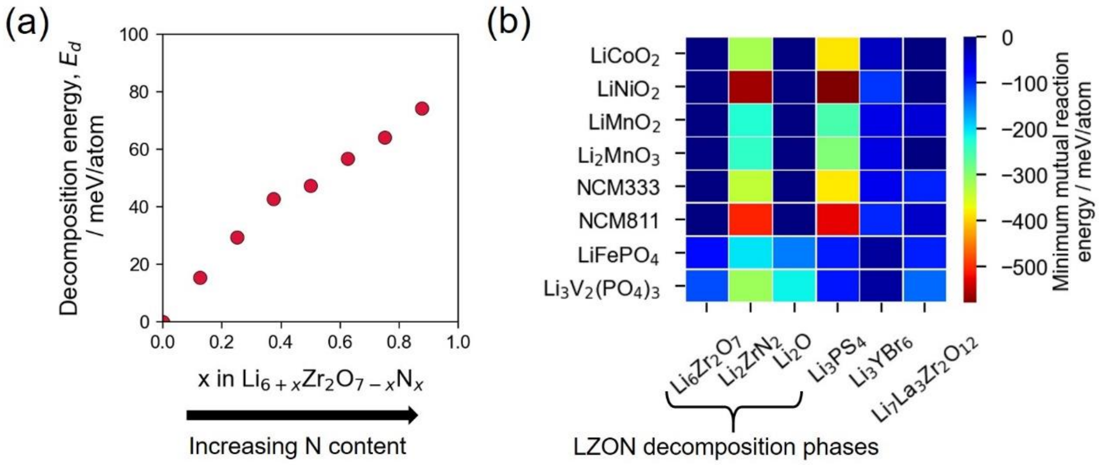

Figure 2. (a) DFT-calculated convex-hull decomposition energy (E_d) vs. N-doping content (x in $Li_{6+x}Zr_2O_{7-x}N_x$, LZON) plot. (b) Thermodynamic-minimum mutual reaction energy heatmap in the pseudo-binary phase diagram related to contact reactivity between known cathode materials (vertical axis) and LZO/LZO-related phases (horizontal axis); known solid electrolytes are included for comparison. Red-to-brown, green-to-yellow and cyan-to-blue color ranges shows the most, moderately and least reactive material combinations, respectively.

Cathode-LZO(N) interface property evaluation

The oxygen-terminated LZO(001) surface is determined to have the lowest $\gamma_{surface}$ (1.14 J/m^2) amongst considered surface structures (Table S1), it is selected here for the construction of an interface model with the low-surface-energy LCO(104). The resulting LCO(104)|LZO(001) interface has a low average strain of 0.79%. The lowest-energy interface-shifted (lateral + vertical) configuration, as found efficiently by our BO+DFT technique after 6 BO steps (Fig. S6), is displayed in Fig. 3a. The interface has all surface Co (Zr) ions of the LCO (LZO) slab topmost layer having adsorbed O ions coming from the LZO (LCO) slab topmost layer, this forms an interlocking configuration of the two material slab surfaces. Additionally, the subsurface Li ions in the LZO slab side are found to relax on top of surface O of the LCO slab topmost layer. These interface atomic rearrangements that result to Li-O, Co-O and Zr-O bond formation are reflected in the visualized differential charge density. The calculated W_{adhesion} value is -1.67 J m^{-2} which indicates strong adhesion. For comparison, W_{adhesion} for well-contacted $Li_7La_3Zr_2O_{12}$-Li, LCO-Li_3PS_4, and LCO-$LiNbO_3$ (LCO-$LiTaO_3$) interfaces are predicted to be -0.98 J m^{-2}, -0.44 J m^{-2}, and -0.79 (-0.82) J m^{-2}, respectively.[49-51]

Fig. 3a (left image) shows the layer-decomposed electronic density of states (LDOS) plots for the six innermost layers of the LCO(104)|LZO(001) interface. There is at least 1 eV band gap observed, suggesting a low likelihood of spontaneous interface electron transfer that would facilitate degradation-related reactions between LCO and LZO upon contact. The valence band maximum (VBM) is characterized by LCO-side (Co-3d, O-2p) electronic states. When LZO acts as a CCL for LCO, the band alignment suggests that during battery charging, electrons are first drawn from LCO side (not from LZO side); this electrochemical process depicts LZO as a stable CCL. There are fewer O-2p states at the highest occupied states, this can be explained by the energy lowering of the O-2p states due to formation of strong interfacial Zr-O bonds. The latter may be beneficial for inhibiting degradation-related reactions (e.g., from O release). The relatively less-negative $\Delta E_{\text{mutual,min}}$ values vs. cathodes of LZO (Fig. 2b) also indicate a similar tendency.

As highlighted in Fig. 2b, there is a relatively severe chemical reactivity vs. known cathodes (i.e., $\Delta E_{\text{mutual,min}} \ll 0$) for $LiZr_2N_2$, a decomposition phase of LZON. Concurrently, the influence of N doping on the interface stability is evaluated by introducing N at the interface and around the LZO(N) bulk region (Fig. 3b, 3c). As shown, the interfacial LDOS profiles can be consequently changed when N is located at the interface, such as the highest occupied states becoming dominated by N-2p states (Fig. 3b). The localized VBM-region states related to Zr–N interaction reflect a significant degree of ionic bonding character. This electronic structure also suggests that electrons can be removed first from the interface during battery charge process, inducing oxidative decomposition. When N is located around the LZO(N) bulk region (Fig. 3c), the N-2p states are pushed down to deeper energy levels, while the highest occupied states are now characterized by LCO-side Co-3d and O-2p states. This should result to a stable interface during cell charging process, similar to the pristine

LCO(104)|LZO(001) interface. Based on DFT total energy comparison between the two interface models, it is found that the configuration with N located away from the interface (Fig. 3c) is energetically more stable (by 3.6 meV atom^{-1}) than the case when N is located at the interface (Fig. 3b). This implies that N does not prefer to segregate to the interface, thus avoiding the interfacial instability related to N-2p states dominating the highest occupied electronic states.

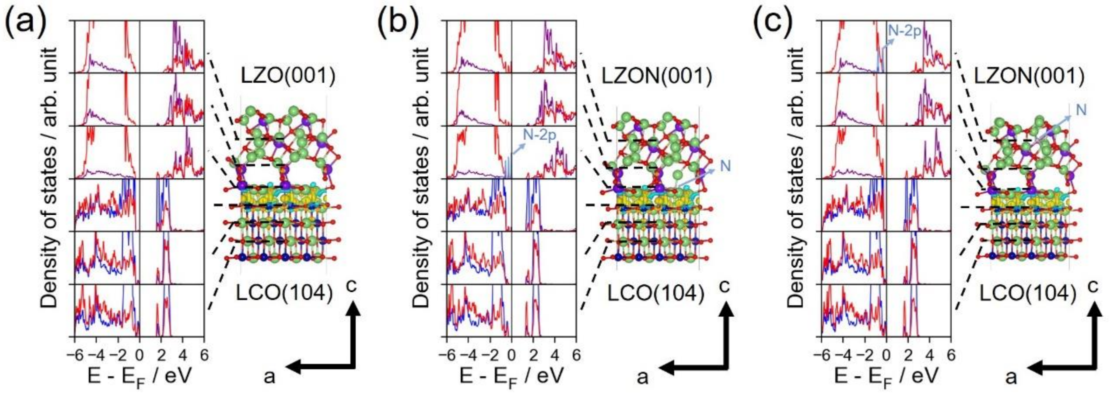

Figure 3. Layered electronic partial density of states (PDOS): (a) pristine LCO(104)|LZO(001) interface, (b) LCO(104)|LZON(001) interface with one N dopant at the interface and (c) LCO(104)|LZON(001) interface with one N dopant away from the interface. Dashed lines represent the corresponding interface layer positions. Charge accumulation (depletion) is shown as yellow (aqua) isosurface; the isosurface level is set at 0.005e Å^{-3}.

Li diffusivity analysis

Fig. 4a, 4b display the bulk Li-ion MSD plots for LZO and LZON from AIMD simulations at various temperatures (600 – 1400 K). The dynamical stability of the LZO (LZON) host framework was confirmed by the flat MSD trends of non-Li ions at all investigated temperatures (Fig. S7, S8). In Fig.4a, a flat Li MSD profile is also observed for LZO, suggesting a negligible $\sigma_{\mathrm{bulk,Li}}$ down to room temperature. In contrast, LZON (i.e., $Li_{6.5}Zr_2O_{6.5}N_{0.5}$) has an increasing MSD slope vs. temperature (Fig. 4b), the extrapolated room-temperature $\sigma_{\mathrm{bulk,Li}}$ is 4.2 x 10^{-5} S cm^{-1}, with an activation energy of 0.32 eV based on the log-diffusivity Arrhenius relationship. The several orders of magnitude increase in conductivity can be explained by the presence of extra Li interstitials from aliovalent N^{3-} anion substitution at the O^{2-} site. Li interstitials in LZO can increase structure entropy by inducing geometric Li site frustration due to the increased local Li-Li repulsion effect from reduced Li-Li average distance. It can energetically penalize specific Li ordering preferences (relative to the pristine case), thus enhancing the overall structure disorder and creating a flatter Li potential energy landscape.[52-53]

To investigate the dependence of $\sigma_{\mathrm{bulk,Li}}$ towards N-doping concentration at 300 K, a machine learning potential based on Sparse Gaussian Process Regression (SGPR) model is trained by AIMD-based energies and forces. The final SGPR potential has been confirmed to have low test dataset errors of 0.9 meV/atom ($R^2 = 0.97$) and 0.09 eV/Å ($R^2 = 0.97$) in energies and forces, respectively (Fig. S10). Stable NPT-MD runs are also verified for the final SGPR potential according to the observed energy, temperature and cell-volume profiles (Fig. S11). Fig. 4c shows the variation of $\sigma_{\mathrm{bulk,Li}}$ at 300 K with respect to N-doping concentration. There is a good agreement between SGPR-based $\sigma_{\mathrm{bulk,Li}}$ (3.9 x 10^{-5} S cm^{-1}) and the AIMD-based extrapolated value (4.2 x 10^{-5} S cm^{-1}) at $x = 0.5$ in $Li_{6+x}Zr_2O_{7-x}N_x$ (i.e., $Li_{6.5}Zr_2O_{6.5}N_{0.5}$).

A maximum $\sigma_{\mathrm{bulk,Li}}$ is determined at $x = 0.25$ (i.e., $Li_{6.25}Zr_2O_{6.75}N_{0.25}$). To explain this optimal composition, two Li-pathway-specific parameters are determined: the largest free sphere diameter along the Li pathway channel (d_1) and the largest included sphere along the free sphere pathway related to the Li pathway channel (d_2).[54] The d_1 parameter is related to the Li pathway bottleneck size which is correlated to the O-O edge distance of the LiO_5 unit (Fig. S12). On the other hand, the d_2 parameter is related to the size of the empty interstitial site relative to the pristine structure (i.e., interstitial Li site-cage size) and along the Li pathway (Fig. S12). It is found that d_1 and d_2 increases and decreases, respectively, with increasing N-doping concentration. The increasing conductivity up to x = 0.25 can then be attributed to the decreasing Li activation energy barrier due to the increasing Li-pathway bottleneck size (i.e., increasing d_1) which decreases steric hindrance during Li jump to the next nearest-neighbor available site. On the other hand, the decreasing conductivity beyond x = 0.25 can be explained by two factors: i) the decreased vibrational and configurational entropy due to decreased available space at the interstitial site (i.e., decreasing d_2) and ii) the decreased number of vacant interstitial jump sites owing to progressive occupancy by extra Li (for charge compensation) when aliovalent N-doping concentration increases. These combined effects can decrease the conductivity prefactor and can account for the observed conductivity decrease for $x > 0.25$. Therefore, for $Li_{6+x}Zr_2O_{7-x}N_x$, Li-pathway bottleneck size, Li site-cage size, and Li (interstitial) vacancy concentration are critical parameters for maximizing conductivity. Li diffusivity activation with N-doping is qualitatively confirmed as well by the observed Li trajectory densities of the N-doped structures which show more connectivity, as compared to the pristine structure (Fig. S13).

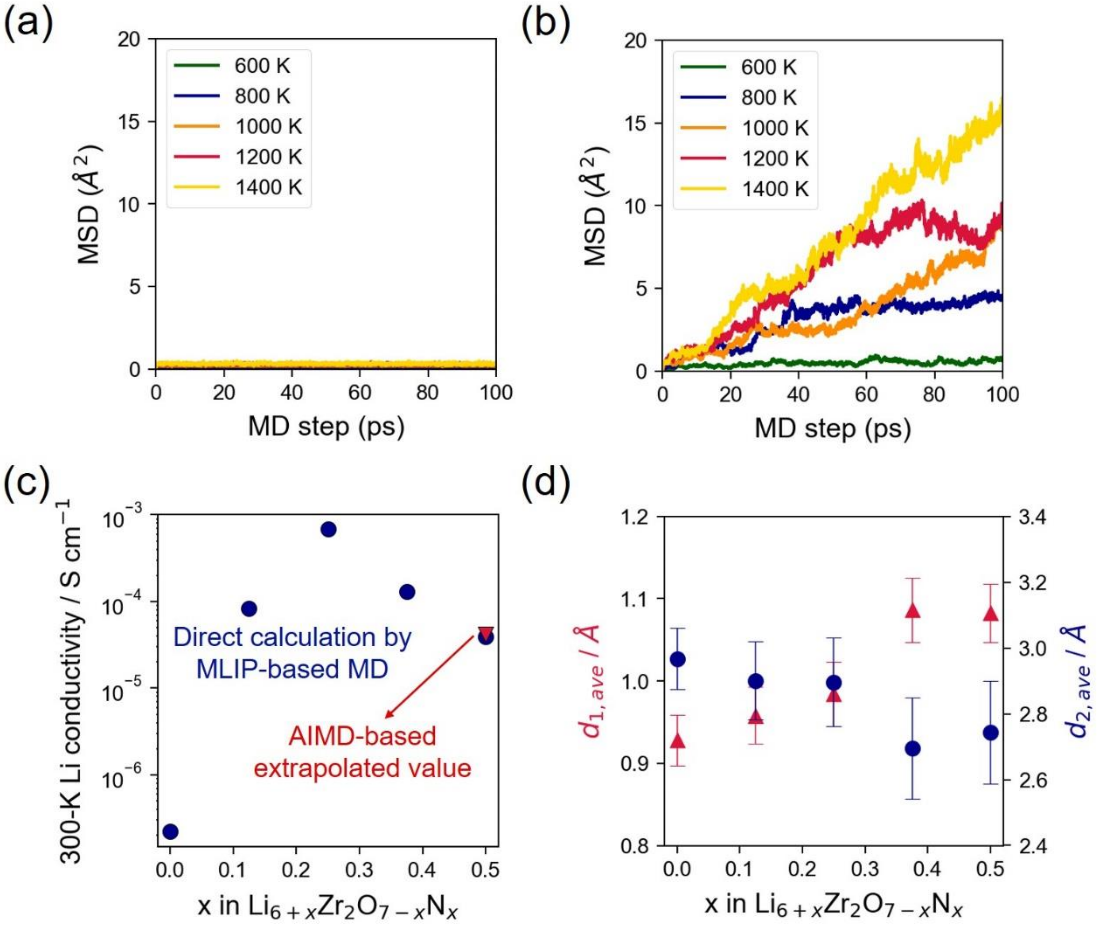

Figure 4. Mean squared displacement (MSD) plots for Li^+ ions from NPT-AIMD simulations (600 – 1400 K): (a) $Li_6Zr_2O_7$ (LZO) and (b) $Li_{6.5}Zr_2O_{6.5}N_{0.5}$ (LZON). (c) Plot for calculated bulk Li conductivity as a function of N-doping content (x in $Li_{6+x}Zr_2O_{7-x}N_x$) by 500-ps direct 300-K MD simulations with a trained machine learning potential (MLIP) based on Sparse Gaussian Process Regression (SGPR). The AIMD-based extrapolated value at 300 K from high-temperature MSD data in (b) is also plotted in (c) for comparison. (d) Plot for geometric-based averaged parameters related to the Li pathway channels in the LZON structure (using the 300-K MLIP-MD trajectories): the largest free sphere diameter along the Li pathway channel (d_1) and the largest included sphere along the free sphere pathway related to the Li pathway channel (d_2). d_1 is related to the Li pathway bottleneck size which is correlated to the O-O edge distance of the LiO_5 unit (Fig. S12), d_2 is related to the size of the empty interstitial site relative to the pristine structure (i.e., interstitial Li site-cage size) and along the Li pathway (Fig. S12).

Fig. 5a and 5b show the $G_{\mathrm{self}}(\boldsymbol{r}, t)$ heatmap for Li ions in LZO and LZON, respectively, as derived from the 1000-K AIMD trajectory data. The typical distance between 1st-nearest neighbor (1NN) Li 8*f* Wyckoff sites is ~3.3 Å while the between the Li 8*f* Wyckoff site and a nearby interstitial site is

~2.3 Å (Fig. 5a inset image). During the high-temperature NPT-AIMD simulation runs in the present work, these characteristic distances are expected to be slightly increased owing to thermal expansion effect. For (pristine) LZO, G_{self} contributions for 1NN distance and beyond are absent because no Li jump events are recorded within the sampled 100-ps trajectory, this is supported as well by the flat Li MSD trends in Fig. 4a. Mainly, only intra-site vibrations are detected as shown by the persistent band at r < 2 Å and the rather disconnected Li trajectory density profile (Fig. 5e). However, because of Li diffusivity activation in LZON by N-doping, significant G_{self} contributions for 1NN distance and beyond are detected such as at bands centered at ~2.6 (1NN), ~5.1 (2NN) and ~7.9 Å (3NN). These $G_{\mathrm{self}}(\boldsymbol{r}, t)$ bands result to a highly connected Li trajectory network (Fig. 5f).

From AIMD trajectories at 1000 K, the characteristic times for Li to move to the 1NN site (τ_1) and the onset for concerted Li migration (τ_2) in the LZON structure are both ~5.1 ps. In the LZO structure, τ_1 and τ_2 values cannot be readily estimated due to the absence of NN Li jump events within 100 ps, thus these parameters are expected to be larger by orders of magnitude than that of the LZON structure. As comparison with the present LZON materials (with predicted Li bulk conductivities in the range of 10^{-4} - 10^{-5} S cm^{-1} at 300 K), τ_1 and τ_2 values derived by the same AIMD simulation approach (at 1000 K) for other reported solid electrolytes in our previous work,[55] such as pyrochlore-type $Li_{1.3125}La_{0.5625}Nb_2O_6F$ (~10^{-3} S cm^{-1}) and garnet-type $Li_7La_3Zr_2O_{12}$ (~10^{-4} S cm^{-1}), are ~1.0 ps (for both latter materials).

Fig. 5c and 5d show the corresponding $G_{\mathrm{distinct}}(\boldsymbol{r}, t)$ heatmaps for Li ions in LZO and LZON, respectively. Since Li ions in LZO are mainly vibrating about their sites, there is no $G_{\mathrm{distinct}}(\boldsymbol{r}, t)$ band for concerted Li ion migration near r = 0, only persistent bands for distinct Li-Li NN distances are noted over MD time. Meanwhile, $G_{\mathrm{distinct}}(\boldsymbol{r}, t)$ build-up near r = 0 is clearly visible for LZON, this confirms that Li ions are moving in a concerted manner within the structure.

The Li correlation length (ξ) was estimated by envelope method from the van hove data at t = 0 (i.e., Li-Li radial distribution function, $g(r)$) from MLIP-MD trajectories at 300 K, based on the form $e^{(-r/\xi)}$;[56] the fitting range was set to 2.7 Å < r < 7.5 Å. It is determined that as the N-doping concentration increases from x = 0 to x = 0.5, ξ decreases from ~6.09 to ~3.57 Å, respectively. The relatively large ξ at x = 0 is due to the preference of Li to keep its ordering that is consistent with its original 8f Wyckoff sites, this is also in agreement with the observed flat Li MSD profiles which show that Li ions are only mainly vibrating at their original sites (Fig. 4a). The value of ξ then decreases as the number of interstitial Li increases due to N-doping, indicating an increase in Li configuration disorder and more Li rearrangement events becoming energetically accessible, this is also supported by the positive MSD slopes of N-doped structures that indicate Li diffusivity activation.

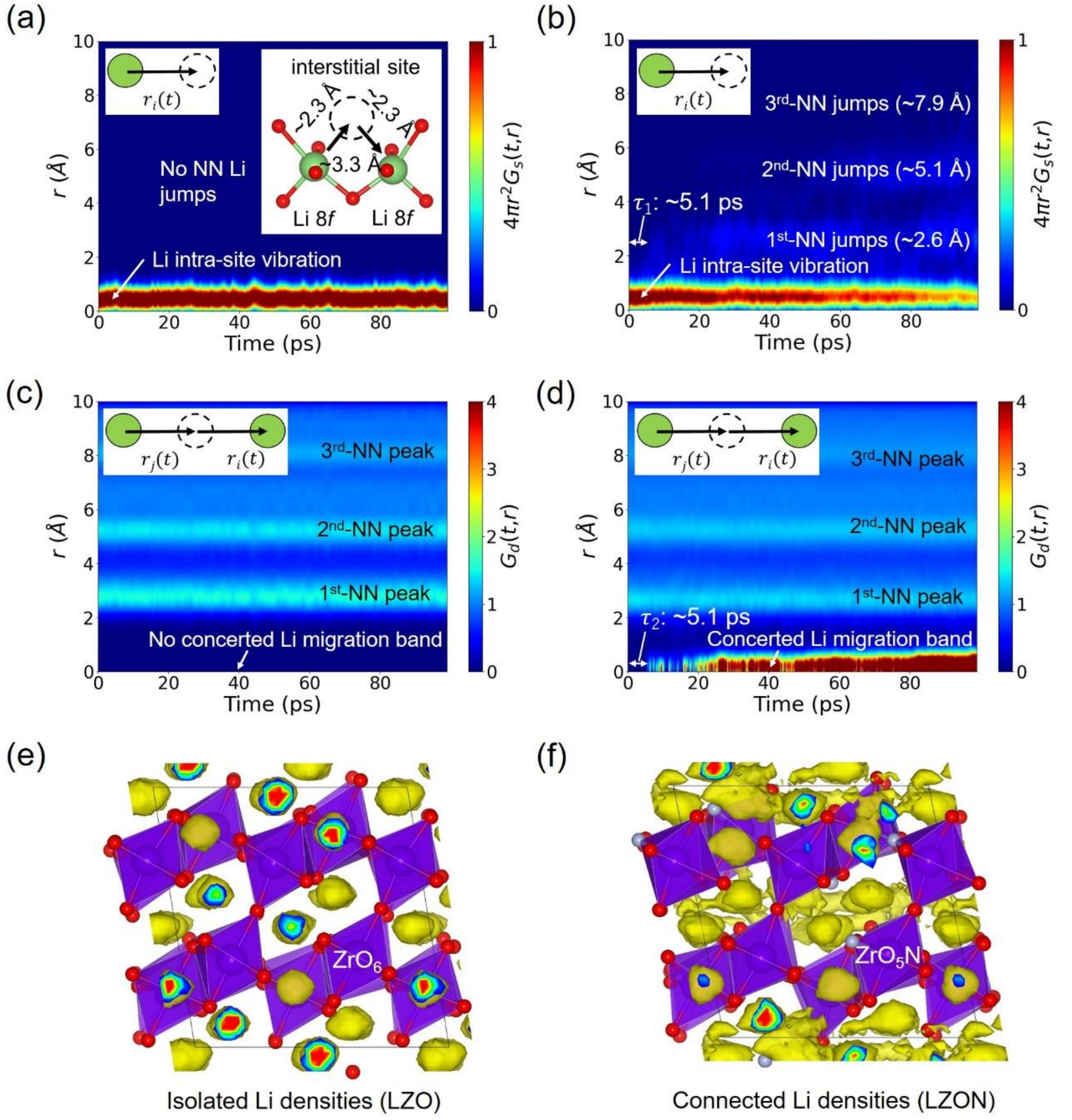

Figure 5. Heatmap profiles for the self (G_{self}) and distinct (G_{distinct}) part of the space-time correlation (van Hove) function derived for Li^+ ions from 1000 K NPT-AIMD trajectories: (a) G_{self} in bulk $Li_6Zr_2O_7$ (LZO), (b) G_{self} in bulk $Li_{6.5}Zr_2O_{6.5}N_{0.5}$ (LZON), (c) G_{distinct} in bulk LZO, and (d) G_{distinct} in bulk LZON. Characteristic nearest-neighbor (NN) Li-Li distances are labeled accordingly. Inset images in (a) shows the schematic picture of G_{self} for a moving Li ion up to a distance described by $r_i(t)$ (dashed circle) and the typical nearest-neighbor site distances (between Li 8*f* Wyckoff sites and between Li 8*f* Wyckoff site and an interstitial Li site) for Li within the LZO crystal structure. The estimated characteristic times for Li to move to the 1st next neighbor (NN) site (τ_1) and the onset for concerted Li migration (τ_2) in the LZON structure are indicated in (b) and (d), respectively, which is $\tau_1 = \tau_2 = \sim 5.1$ ps. Inset images in (c) and (d) display the schematic picture for G_{distinct} related to Li_i and Li_j described by $r_i(t)$ and $r_j(t)$, respectively, with respect to a formerly occupied

vacancy/interstitial site/position (dashed circle). The corresponding Li trajectory densities are shown in (e) and (f) for LZO and LZON, respectively (isosurface: blue (low count) → red (high count)); Zr atoms and $Zr(O,N)_6$ polyhedral units are shown in purple, O atoms in red, N atoms in light blue color). Li atoms are not shown for visual clarity.

Li transport across the cathode-coating interface

Several local Li ion migration pathways across the LCO(104)|LZO(001) interface are evaluated by DFT-cNEB method (Fig. 6a). On the LCO(104) surface, two initial Li states are identified based on local environment: LiO_6 (I_1) and LiO_5 (I_2) coordination. For each distinct initial state, several final states in different directions toward the LZO side are sampled (i.e., [path $I_{1\text{-}1}$, path $I_{1\text{-}2}$] and [path $I_{2\text{-}1}$, path $I_{2\text{-}2}$, path $I_{2\text{-}3}$], respectively); the Li final states are similarly LiO_5-coordinated as those in bulk LZO (Fig. 1b). The migration energy profiles (Fig. 6b) show that there are local variations in Li site energy based on the difference between initial and final state energies. The energy difference is in the range of 0.2 – 0.5 eV range, with no clear tendency as to which slab side (i.e., LCO or LZO) has the consistently higher (or lower) relative energy. This trend can be explained largely by the interface being formed by two similar materials (i.e., both are oxides, similar Li-O bonding nature in the two materials). Previous DFT predictions on LCO|Li_3PS_4 interface which is formed by two dissimilar materials (i.e., oxide and sulfide, Li-O vs. Li-S bonding nature) showed that Li ions in the Li_3PS_4 slab have a consistently higher Li site energy than in the LCO slab side, reflecting a significant difference in the Li chemical potential alignment across the interface.[50]

Of the sampled local migration pathways across the LCO(104)|LZO(001) interface, a minimum Li ion migration energy is found in path $I_{2\text{-}3}$ which has 0.40 and 0.27 eV in the forward and the backward direction, respectively. These values are comparable with the bulk Li ion migration energy of LCO (0.20 – 0.60 eV) for a vacancy-driven migration process.[57] This pathway is characterized by similarly coordinated initial and final states (i.e., LiO_5-to-LiO_5 pathway). Its relatively low barrier is owed to its saddle point location which is near an empty region (marked as * in Fig. 3b lower inset image), resulting to a low electrostatic repulsion for the moving Li. Conversely, the other pathways have inequivalent initial and final state coordination, such as path $I_{1\text{-}1}$ (i.e., LiO_6-to-LiO_5 pathway). The latter's saddle point is located along an O-O edge (Fig. 3b upper inset image) which is geometrically restricting for a moving Li, as evidenced by the calculated barriers which are 0.80 and 0.60 eV in the forward and the backward direction, respectively.

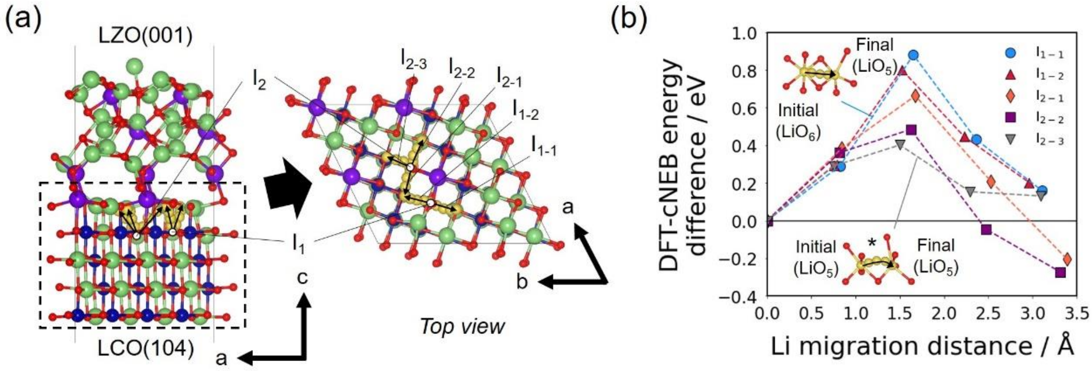

Figure 6. (a) Sampled local Li ion migration pathways (each highlighted as a series of yellow spheres marked by a black arrow) at the interface region formed by $LiCoO_2$(104) (LCO(104)) and $Li_6Zr_2O_7$(001) (LZO(001)) by DFT climbing-image nudged elastic band (DFT-cNEB) method. Li, Co, Zr, O atoms are shown in green, blue, purple and red, respectively. Initial image states (I_1, I_2) from the LCO side are distinguished by white circles, while final image states are shown by the black arrow heads ($I_{1\text{-}1}$, $I_{1\text{-}2}$ for local pathways that start from I_1; $I_{2\text{-}1}$, $I_{2\text{-}2}$, $I_{2\text{-}3}$ for local pathways that start from I_2). State I_1 has the moving Li ion initially in an LiO_6 configuration, while state I_2 has the moving Li ion initially in an LiO_5 configuration. (b) DFT-cNEB Li ion migration energy profiles of sampled local Li pathways. Inset images correspond to visualized Li pathways for $I_{1\text{-}1}$ and $I_{2\text{-}3}$.

Discussion

LZO is predicted as a ground-state phase and it does not readily decompose when in contact with most cathodes, such as LCO. On the other hand, LZON is evaluated to be a metastable phase and chemically reactive with most cathodes based on bulk reactivity analysis (i.e., $\Delta E_{\mathrm{mutual,min}} << 0$). From this thermodynamic point of view, LZON is less appealing when directly applied to the cathode surface as a CCL. However, if LZON can be kinetically stabilized, this reactivity issue can be addressed.

The predicted low strain and strong interface adhesion of the LCO(104)|LZO(001) interface indicate that a good CCL contact can be realized for this material pair. The strong interfacial Co-O (Zr-O) bonding could help stabilize the cycling even of Ni-rich layered cathodes (e.g., NCM333, NCM811 and $LiNiO_2$) which are prone to degradation due to large volume changes associate with Li (de-)intercalation.[58] The LDOS profiles show that the LCO(104)|LZO(001) interface VBM is contributed by LCO-side electronic states. Therefore, a typical charging process can be facilitated with this interface contact (i.e., electrons can be extracted first from LCO and not from LZO). In the case of LZON, interfacial instability is also found to be less likely due to the energetic preference of N dopant to stay around the LZO(N) bulk region, this results to a similar interfacial electronic structure as with the LCO(104)|LZO(001) interface. When N resides at the interface, N-2p states appear at the highest occupied states, favoring an LZON-side electron removal process, especially at first-cycle charging, that can serve as the onset for the formation of bulk-related oxidative decomposition products (Fig. 2b). When compared to other CCL materials such as $LiNbO_3$ and $LiTaO_3$,[51] LZO (or LZON with x = 0.125) is evaluated to provide a relatively more strongly adhered interface, the interface work of adhesion values are -0.79, -0.82 and -1.67 (1.66) J/m^2, respectively. The stronger contact of LZO (LZON) is expected to promote better cycling performance, such as by minimizing contact loss. Meanwhile, the three mentioned CCL materials demonstrate a similar interfacial electronic structure when interfaced with LCO at pre-charging condition, in which there are fewer O high-energy states at the interface near the highest-occupied states because of the interfacial Nb/Ta/Zr-O bond effectively lowering the energy of O 2p states. This energy lowering of O 2p states can suppress oxygen activity (e.g., oxygen release) in the interface region. Therefore, $LiNbO_3$, $LiTaO_3$ and LZO (or LZON), as CCL materials, can largely minimize LCO degradation over the course cell cycling.

The $\sigma_{\text{bulk,Li}}$ of LZON (~10^{-5} S cm^{-1}, at x = 0.5 in $Li_{6+x}Zr_2O_{7-x}N_x$), as estimated by AIMD method, confirms that N doping is a viable strategy to activate the Li ion transport in LZO. However, for practical SE application, LZON must be further optimized to reach the order of 10^{-3} S cm^{-1} or higher. With LCO cathode, this optimization effort is worth pursuing, given that a stable interface and an enhanced Li diffusivity can be realized with LZON, without the need for an additional CCL or interface buffer layer. Meanwhile, bulk LZO does not demonstrate high Li diffusivity, but for CCL use Li ions can still cross the hetero-interface with reasonably low migration barrier (i.e., 0.40 and 0.27 eV for forward and backward direction, respectively, see Fig. 6b). As previously noted, these aforementioned findings are consistent with the experimental report on improved cycling properties of cathodes with LZO CCL.[16]

The reported low experimental Li ion conductivity in LZO at elevated temperature (573 K, Ref. 18-19) is in good agreement with our AIMD simulations results, in particular with the 600-K MSD plot for Li ions which has a generally flat trend within 100 ps (see Fig. 4a), indicating that most Li ions fail to migrate to the next-neighbor sites and that they are mainly exhibiting vibrational motion only around their initial sites. The large experimental activation energy of LZO can be explained by the extra energy penalty arising from Li vacancy/interstitial creation (i.e., defect energy formation energy contribution to the activation energy) which is needed before the actual Li ion conduction process could occur.[59] The contribution of grain boundary resistance towards total conductivity can also become significant especially in oxide-type solid electrolytes due to possible secondary phases and the need for high sintering temperature to obtain their highly-dense pellet form.[60-62]

The possible synthesis methods for LZON are those reported for LiPON solid electrolytes, given the similarity of their base materials (oxides). For example, one experimental report has shown that bulk crystalline LiPON can be successfully prepared via mechano-synthesis from precursors such as $LiPO_3$ and Li_3N.[63] The possible precursors then for LZON would be LZO and Li_3N. Another possible approach to prepare LZON is by solution-based synthesis, as demonstrated in one report in which bulk LiPON was prepared through stepwise reduction process between precursors lithium tert-butoxide (LiOtBu) and diethyl phosphoramidate (DEPA) precursors.[64] LZON may also be prepared by deposition techniques, as reported in the case of LiPON.[65] Meanwhile, the effect of nitriding process on the crystallinity of LZON is expected to be strongly dependent on process parameters. For example, nitriding process can initially result to the formation of amorphous LZON phase, the crystallinity of the latter can be increased by prolonged heat treatments. The degree of crystallinity can affect the ionic conductivity, depending on the crystallized phase or secondary phase formation.[63] There are no experimental reports yet related to the sintering temperature of LZON but if it behaves similarly to LiPON, then its sintering temperature can be relatively low (i.e., below ~700 K to avoid irreversible N loss),[63] as compared to other oxide-based solid electrolytes such as NASICON-type LATP and garnet-type $Li_7La_3Zr_2O_{12}$ (1200 – 1500 K).[66-67]

Conclusion

The present study has comprehensively evaluated the thermodynamic, electrochemical and Li diffusion properties of LZO in terms of bulk and cathode-contact interface. Based on grand-canonical free energy calculations, LZO has a low reactivity with known cathode materials such as LCO and even degradation-prone Ni-rich layered compounds (NCM333, NCM811 and $LiNiO_2$). A low-energy $LiCoO_2$(104)|LZO(001) interface structure was successfully searched by BO+DFT technique which is characterized by a strongly adhered interface contact with low strain. This interface is remarkably stable and has an electronic structure that can facilitate stable cell cycling. Moreover, DFT-cNEB results show that the LCO(104)|LZO(001) interface has interface-normal local diffusion pathways with low Li ion migration energy. These interfacial properties are consistent with the observed enhancement of the capacity retention reported for cathodes LZO CCL. AIMD and MLIP-MD data shows that Li diffusivity in bulk LZO can be significantly increased by several orders of magnitude through N-doping which activates the Li-interstitial diffusion mechanism. For the LCO(104)|LZON(001) interface, the N dopant is found to be more energetically stable at the LZON bulk region, not at the interface. This preference results to an interface electronic structure with LCO-side states (Co-3d, O-2p) dominating the highest occupied states, similar to the LCO(104)|LZO(001) interface. Consequently, a stable cell charging can be expected as well for the LZON as the CCL material.

Acknowledgments

RJ is thankful for the financial support in part by JST through Green Technologies of Excellence (GteX) grant number JPMJGX23S2, by JSPS KAKENHI grant number JP21K14729, as well as MEXT as Materials Processing Science project ("Materealize") grant number JPMXP0219207397 and the "Program for Promoting Research on the Supercomputer Fugaku" grant number JPMXP1020230325. The calculations were carried out both in NIMS supercomputer (Numerical Materials Simulator) and the Fugaku supercomputer at the RIKEN through the HPCI System Research Project (project ID: hp240118, hp210105). The VESTA software was used for crystal structure visualization.[68] The python Matplotlib package was used for generating the plots.[69]

References

1. Knauth, P., Inorganic solid Li ion conductors: An overview. *Solid State Ionics* **2009,** *180* (14-16), 911-916.

2. Takada, K., Progress in solid electrolytes toward realizing solid-state lithium batteries. *J Power Sources* **2018,** *394*, 74-85.

3. Murugan, R.; Thangadurai, V.; Weppner, W., Fast lithium ion conduction in garnet-type Li7La3Zr2O12. *Angew Chem Int Edit* **2007,** *46* (41), 7778-7781.

4. Lee, T.; Qi, J.; Gadre, C. A.; Huyan, H. X.; Ko, S. T.; Zuo, Y. X.; Du, C. J.; Li, J.; Aoki, T.; Wu, R. Q.; Luo, J.; Ong, S. P.; Pan, X. Q., Atomic-scale origin of the low grain-boundary resistance in perovskite solid electrolyte $Li_{0.375}Sr_{0.4375}Ta_{0.75}Zr_{0.25}O_3$. *Nat Commun* **2023,** *14* (1).

5. Mertens, A.; Yu, S. C.; Schön, N.; Gunduz, D. C.; Tempel, H.; Schierholz, R.; Hausen, F.; Kungl, H.; Granwehr, J.; Eichel, R. A., Superionic bulk conductivity in $Li_{1.3}Al_{0.3}Ti_{1.7}(PO_4)_3$ solid electrolyte. *Solid State Ionics* **2017,** *309*, 180-186.

6. Feng, J. K.; Lu, L.; Lai, M. O., Lithium storage capability of lithium ion conductor $Li_{1.5}Al_{0.5}Ge_{1.5}(PO_4)_3$. *J Alloy Compd* **2010,** *501* (2), 255-258.

7. Tanaka, Y.; Ueno, K.; Mizuno, K.; Takeuchi, K.; Asano, T.; Sakai, A., New Oxyhalide Solid Electrolytes with High Lithium Ionic Conductivity >10 mS cm^{-1} for All-Solid-State Batteries. *Angew Chem Int Edit* **2023,** *62* (13).

8. Aimi, A.; Onodera, H.; Shimonishi, Y.; Fujimoto, K.; Yoshida, S., High Li-Ion Conductivity in Pyrochlore-Type Solid Electrolyte $Li_{2-x}La_{(1+x)/3}M_2O_6F$ (M = Nb, Ta). *Chem Mater* **2024**, 36, 8, 3717-3725.

9. Nishio, K.; Imazeki, D.; Kurushima, K.; Takeda, Y.; Edamura, K.; Nakayama, R.; Shimizu, R.; Hitosugi, T., Immense Reduction in Interfacial Resistance between Sulfide Electrolyte and Positive Electrode. *Acs Appl Mater Inter* **2022,** *14* (30), 34620-34626.

10. Ohta, S.; Seki, J.; Yagi, Y.; Kihira, Y.; Tani, T.; Asaoka, T., Co-sinterable lithium garnet-type oxide electrolyte with cathode for all-solid-state lithium ion battery. *J Power Sources* **2014,** *265*, 40-44.

11. Han, X. G.; Gong, Y. H.; Fu, K.; He, X. F.; Hitz, G. T.; Dai, J. Q.; Pearse, A.; Liu, B. Y.; Wang, H.; Rublo, G.; Mo, Y. F.; Thangadurai, V.; Wachsman, E. D.; Hu, L. B., Negating interfacial impedance in garnet-based solid-state Li metal batteries. *Nat Mater* **2017,** *16* (5), 572-579.

12. Wang, C. W.; Gong, Y. H.; Liu, B. Y.; Fu, K.; Yao, Y. G.; Hitz, E.; Li, Y. J.; Dai, J. Q.; Xu, S. M.; Luo, W.; Wachsman, E. D.; Hu, L. B., Conformal, Nanoscale ZnO Surface Modification of Garnet-Based

Solid-State Electrolyte for Lithium Metal Anodes. *Nano Lett* **2017,** *17* (1), 565-571.

13. Song, J. H.; Zhang, C.; Zheng, Z. J.; Huo, S. Z.; Lin, Y. H.; Yang, F.; Liu, L., Construction of SnO2 buffer layer and analysis of its interface modification for Li and Li1.5Al0.5Ge1.5(PO4)3 in solid-state batteries. *J Colloid Interf Sci* **2024,** *663*, 132-142.

14. Singh, D. P.; Birkhölzer, Y. A.; Cunha, D. M.; Dubbelink, T.; Huang, S. Z.; Hendriks, T. A.; Lievens, C.; Huijben, M., Enhanced Cycling and Rate Capability by Epitaxially Matched Conductive Cubic TiO Coating on $LiCoO_2$ Cathode Films. *Acs Appl Energ Mater* **2021,** *4* (5), 5024-5033.

15. Ohta, N.; Takada, K.; Sakaguchi, I.; Zhang, L. Q.; Ma, R. Z.; Fukuda, K.; Osada, M.; Sasaki, T., $LiNbO_3$-coated $LiCoO_2$ as cathode material for all solid-state lithium secondary batteries. *Electrochem Commun* **2007,** *9* (7), 1486-1490.

16. Yang, H. P.; Li, L. J.; Liu, C. Y.; Chen, J.; Xia, L. F.; Liu, Z. S.; Chen, J. X.; Chen, Z. Y.; Duan, J. F., Simultaneous synthesis and synergetic stabilization of Zr-doped and $Li_6Zr_2O_7$-coated Ni-rich layered cathode for advanced lithium ion batteries. *Electrochim Acta* **2020,** *364*.

17. Manthiram, A.; Knight, J. C.; Myung, S. T.; Oh, S. M.; Sun, Y. K., Nickel-Rich and Lithium-Rich Layered Oxide Cathodes: Progress and Perspectives. *Adv Energy Mater* **2016,** *6* (1).

18. Rao, R. P.; Reddy, M. V.; Adams, S.; Chowdari, B. V. R., Preparation and mobile ion transport studies of Ta and Nb doped $Li_6Zr_2O_7$ Li-fast ion conductors. *Mater Sci Eng B-Adv* **2012,** *177* (1), 100-105.

19. Liao, Y. H.; Singh, P.; Park, K. S.; Li, W. S.; Goodenough, J. B., $Li_6Zr_2O_7$ interstitial lithium-ion solid electrolyte. *Electrochim Acta* **2013,** *102*, 446-450.

20. Chae, M. S., Lithium migration mechanism in lithium zirconium oxide coating layers for all-solid-state lithium batteries. *J Solid State Chem* **2024,** *337*.

21. Kresse, G., Ab-Initio Molecular-Dynamics for Liquid-Metals. *J Non-Cryst Solids* **1995,** *193*, 222-229.

22. Kresse, G.; Furthmuller, J., Efficient iterative schemes for ab initio total-energy calculations using a plane-wave basis set. *Phys Rev B* **1996,** *54* (16), 11169-11186.

23. Perdew, J. P.; Wang, Y., Accurate and Simple Analytic Representation of the Electron-Gas Correlation-Energy. *Phys Rev B* **1992,** *45* (23), 13244-13249.

24. Kresse, G.; Joubert, D., From ultrasoft pseudopotentials to the projector augmented-wave method. *Phys Rev B* **1999,** *59* (3), 1758-1775.

25. Blochl, P. E., Projector Augmented-Wave Method. *Phys Rev B* **1994,** *50* (24), 17953-17979.

26. Perdew, J. P.; Burke, K.; Ernzerhof, M., Generalized gradient approximation made simple. *Phys Rev Lett* **1996,** *77* (18), 3865-3868.

27. Perdew, J. P.; Ruzsinszky, A.; Csonka, G. I.; Vydrov, O. A.; Scuseria, G. E.; Constantin, L. A.; Zhou, X. L.; Burke, K., Restoring the density-gradient expansion for exchange in solids and surfaces. *Phys Rev Lett* **2008,** *100* (13).

28. Czekalla, R.; Jeitschko, W., Preparation and Crystal-Structure of Li6zr2o7 and Li6hf2o7. *Z*

Anorg Allg Chem **1993,** *619* (12), 2038-2042.

29. Johnston, W. D.; Heikes, R. R.; Sestrich, D., The Preparation, Crystallography, and Magnetic Properties of the $Li_xCo_{(1-X)}O$ System. *J Phys Chem Solids* **1958,** *7* (1), 1-13.

30. Wang, L.; Maxisch, T.; Ceder, G., Oxidation energies of transition metal oxides within the GGA+U framework. *Phys Rev B* **2006,** *73* (19).

31. Monkhorst, H. J.; Pack, J. D., Special Points for Brillouin-Zone Integrations. *Phys Rev B* **1976,** *13* (12), 5188-5192.

32. Shen, J. X.; Horton, M.; Persson, K. A., A charge-density-based general cation insertion algorithm for generating new Li-ion cathode materials. *Npj Comput Mater* **2020,** *6* (1).

33. Ong, S. P.; Wang, L.; Kang, B.; Ceder, G., Li-Fe-P-O-2 phase diagram from first principles calculations. *Chem Mater* **2008,** *20* (5), 1798-1807.

34. Zhu, Y. Z.; He, X. F.; Mo, Y. F., First principles study on electrochemical and chemical stability of solid electrolyte-electrode interfaces in all-solid-state Li-ion batteries. *J Mater Chem A* **2016,** *4* (9), 3253-3266.

35. Jain, A.; Ong, S. P.; Hautier, G.; Chen, W.; Richards, W. D.; Dacek, S.; Cholia, S.; Gunter, D.; Skinner, D.; Ceder, G.; Persson, K. A., Commentary: The Materials Project: A materials genome approach to accelerating materials innovation. *Apl Mater* **2013,** *1* (1).

36. Ong, S. P.; Richards, W. D.; Jain, A.; Hautier, G.; Kocher, M.; Cholia, S.; Gunter, D.; Chevrier, V. L.; Persson, K. A.; Ceder, G., Python Materials Genomics (pymatgen): A robust, open-source python library for materials analysis. *Comp Mater Sci* **2013,** *68*, 314-319.

37. Qian, D. N.; Hinuma, Y.; Chen, H. L.; Du, L. S.; Carroll, K. J.; Ceder, G.; Grey, C. P.; Meng, Y. S., Electronic Spin Transition in Nanosize Stoichiometric Lithium Cobalt Oxide. *J Am Chem Soc* **2012,** *134* (14), 6096-6099.

38. Zur, A.; Mcgill, T. C., Lattice Match - an Application to Heteroepitaxy. *J Appl Phys* **1984,** *55* (2), 378-386.

39. Mockus, J. B.; Mockus, L. J., Bayesian-Approach to Global Optimization and Application to Multiobjective and Constrained Problems. *J Optimiz Theory App* **1991,** *70* (1), 157-172.

40. Hoover, W. G.; Ladd, A. J. C.; Moran, B., High-Strain-Rate Plastic-Flow Studied Via Non-Equilibrium Molecular-Dynamics. *Phys Rev Lett* **1982,** *48* (26), 1818-1820.

41. Willow, S. Y.; Hajibabaei, A.; Ha, M.; Yang, D. C.; Myung, C. W.; Min, S. K.; Lee, G. S.; Kim, K. S., Sparse Gaussian process based machine learning first principles potentials for materials simulations: Application to batteries, solar cells, catalysts, and macromolecular systems. *Chem Phys Rev* **2024,** *5* (4).

42. Hajibabaei, A.; Myung, C. W.; Kim, K. S., Sparse Gaussian process potentials: Application to lithium diffusivity in superionic conducting solid electrolytes. *Phys Rev B* **2021,** *103* (21).

43. Hajibabaei, A.; Kim, K. S., Universal Machine Learning Interatomic Potentials: Surveying Solid Electrolytes. *J Phys Chem Lett* **2021,** *12* (33), 8115-8120.

44. Ha, M.; Hajibabaei, A.; Kim, D. Y.; Singh, A. N.; Yun, J.; Myung, C. W.; Kim, K. S., Al-Doping Driven Suppression of Capacity and Voltage Fadings in 4d-Element Containing Li-Ion-Battery Cathode Materials: Machine Learning and Density Functional Theory. *Adv Energy Mater* **2022,** *12* (30).

45. He, Y.; Burov, S.; Metzler, R.; Barkai, E., Random time-scale invariant diffusion and transport coefficients. *Phys Rev Lett* **2008,** *101* (5).

46. Atkins, P., *Atkins' Physical Chemistry*. 11 ed.; Oxford University Press: 2006; p 1040.

47. Nitzan, A., *Chemical Dynamics in Condensed Phases: Relaxation, Transfer and Reactions in Condensed Molecular Systems*. Oxford Graduate Texts; Oxford University Press: Oxford: 2006.

48. Sun, W. H.; Dacek, S. T.; Ong, S. P.; Hautier, G.; Jain, A.; Richards, W. D.; Gamst, A. C.; Persson, K. A.; Ceder, G., The thermodynamic scale of inorganic crystalline metastability. *Sci Adv* **2016,** *2* (11).

49. Gao, B.; Jalem, R.; Tateyama, Y., Surface-Dependent Stability of the Interface between Garnet $Li_7La_3Zr_2O_{12}$ and the Li Metal in the All-Solid-State Battery from First-Principles Calculations. *Acs Appl Mater Inter* **2020,** *12* (14), 16350-16358.

50. Gao, B.; Jalem, R.; Ma, Y. M.; Tateyama, Y., Li

Transport Mechanism at the Heterogeneous Cathode/Solid Electrolyte Interface in an All-Solid-State Battery via the First-Principles Structure Prediction Scheme. *Chem Mater* **2020,** *32* (1), 85-96.

51. Zhou, Z. Z.; Luong, H. D.; Gao, B.; Momma, T.; Tateyama, Y., $LiNbO_3$ and $LiTaO_3$ Coating Effects on the Interface of the $LiCoO_2$ Cathode: A DFT Study of Li-Ion Transport. *Acs Appl Mater Inter* **2024,** *16* (32), 42093-42099.

52. Jalem, R.; Natsume, R.; Nakayama, M.; Kasuga, T., First-Principles Investigation of the Na+ Ion Transport Property in Oxyfluorinated Titanium(IV) Phosphate $Na_3Ti_2P_2O_{10}F$. *J Phys Chem C* **2016,** *120* (3), 1438-1445.

53. Morgan, B. J., Lattice-geometry effects in garnet solid electrolytes: a lattice-gas Monte Carlo simulation study. *Roy Soc Open Sci* **2017,** *4* (11).

54. Willems, T. F.; Rycroft, C.; Kazi, M.; Meza, J. C.; Haranczyk, M., Algorithms and tools for high-throughput geometry-based analysis of crystalline porous materials. *Micropor Mesopor Mat* **2012,** *149* (1), 134-141.

55. Jalem, R.; Takada, K.; Onodera, H.; Yoshida, S., Crystal structure, stability and Li superionic conductivity of pyrochlore-type solid electrolyte $Li_{2-x}La_{(1+x)/3}Nb_2O_6F$: a first-principles calculation study. *J Mater Chem A* **2024,** *12* (47), 33099-33113.

56. Li, Z. L.; Chen, J. X.; Ding, Z. W.; Wang, Y. B.; Liu, J. Q.; Bian, X. B., Linking high-order harmonic generation and radial distribution function in liquids. *Phys Rev A* **2024,** *110* (4).

57. Van der Ven, A.; Ceder, G., Lithium diffusion in layered Li_xCoO_2. *Electrochem Solid St* **2000,** *3* (7), 301-304.

58. Kim, J.; Lee, H.; Cha, H.; Yoon, M.; Park, M.; Cho, J., Prospect and Reality of Ni-Rich Cathode for Commercialization. *Adv Energy Mater* **2018,** *8* (6).

59. Sebastian, L.; Gopalakrishnan, J.; Piffard, Y., Synthesis, crystal structure and lithium ion conductivity of LiMgFSO. *J Mater Chem* **2002,** *12* (2), 374-377.

60. Lee, R. H.; Kang, C. Y.; Lee, J. K.; Jin, B. S.; Kim, K. N.; Kim, H. S.; Yoon, J. R.; Lee, S. H., Tailoring the grain boundary structure and chemistry of the dendrite-free garnet solid electrolyte $Li_{6.1}Ga_{0.3}La_3Zr_2O_{12}$. *Npg Asia Mater* **2024,** *16* (1).

61. Park, C.; Na, S.; Park, H. G.; Park, K., Synergistic Effect of Calcination and Sintering on the Reduction of Grain Boundary Resistance of LATP Solid Electrolyte. *Acs Appl Mater Inter* **2023,** *15* (22), 26985-26992.

62. Ma, C.; Chen, K.; Liang, C. D.; Nan, C. W.; Ishikawa, R.; More, K.; Chi, M. F., Atomic-scale origin of the large grain-boundary resistance in perovskite Li-ion-conducting solid electrolytes. *Energ Environ Sci* **2014,** *7* (5), 1638-1642.

63. López-Aranguren, P.; Reynaud, M.; Gluchowski, P.; Bustinza, A.; Galceran, M.; del Amo, J. M. L.; Armand, M.; Casas-Cabanas, M., Crystalline LiPON as a Bulk-Type Solid Electrolyte. *Acs Energy Lett* **2021,** *6* (2), 445-450.

64. Gomez, O. J.; Antar, A.; Hall, A. T.; Tapia-Aracayo, L.; Seo, J.; Kim, N.; Sun, Z. H.; Lim, R.; Chen, F.; Li, Y.; Cumings, J.; Rubloff, G.; Lee, S. B.; Stewart, D.; Wang, Y., A facile synthesis of bulk LiPON in solution for solid-state electrolytes. *J Mater Chem A* **2025,** *13* (34), 28368-28376.

65. Inoue, M.; Iwane, H.; Kikuyama, H.; Tasaki, Y.; Honda, Y.; Abe, T., Preparation of highly ionic conductive lithium phosphorus oxynitride electrolyte particles using the polygonal barrel-plasma treatment method. *J Alloy Compd* **2022,** *923*.

66. Yan, G.; Yu, S. C.; Nonemacher, J. F.; Tempel, H.; Kungl, H.; Malzbender, J.; Eichel, R. A.; Krüger, M., Influence of sintering temperature on conductivity and mechanical behavior of the solid electrolyte LATP. *Ceram Int* **2019,** *45* (12), 14697-14703.

67. Huang, M. A.; Liu, T.; Deng, Y. F.; Geng, H. X.; Shen, Y.; Lin, Y. H.; Nan, C. W., Effect of sintering temperature on structure and ionic conductivity of $Li_{7-x}La_3Zr_2O_{12-0.5x}$ (x=0.5~0.7) ceramics. *Solid State Ionics* **2011,** *204*, 41-45.

68. Momma, K.; Izumi, F., for three-dimensional visualization of crystal, volumetric and morphology data. *J Appl Crystallogr* **2011,** *44*, 1272-1276.

69. Hunter, J. D., Matplotlib: A 2D graphics environment. *Comput Sci Eng* **2007,** *9* (3), 90-95.

Graphical Abstract